Biophysical Journal Volume 90 March 2006 2038–2050

SARS Coronavirus E Protein in Phospholipid Bilayers: An X-Ray Study

Z. Khattari,* G. Brotons,* M. Akkawi,† E. Arbely,‡ I. T. Arkin,‡ and T. Salditt*
*Institute for X-ray Physics, University of Göttingen, Göttingen, Germany; †Faculty of Science and Technology, Al-Quds University, Abu Dis, Jerusalem, Israel; and ‡Alexander Silberman Institute of Life Sciences, Department of Biological Chemistry, The Hebrew University of Jerusalem, Givat-Ram, Jerusalem, Israel

ABSTRACT We investigated the structure of the hydrophobic domain of the severe acute respiratory syndrome E protein in model lipid membranes by x-ray reflectivity and x-ray scattering. In particular, we used x-ray reflectivity to study the location of an iodine-labeled residue within the lipid bilayer. The label imposes spatial constraints on the protein topology. Experimental data taken as a function of protein/lipid ratio *P/L* and different swelling states support the hairpin conformation of severe acute respiratory syndrome E protein reported previously. Changes in the bilayer thickness and acyl-chain ordering are presented as a function of *P/L*, and discussed in view of different structural models.

INTRODUCTION

The severe acute respiratory syndrome (SARS) that broke out in April 2003 is a newly identified infectious disease (1–5). The coronavirus (SARS-CoV) has been identified as the primary causative agent for SARS. Sequence analysis reveals the phylogeny of SARS-CoV, showing characteristic features of a coronavirus. At the same time it belongs to a new group that is sufficiently different from known coronaviruses (6,7). Coronaviruses have four important viral genes with different structural proteins: a spike glycoprotein (S), a small envelope protein (E), a matrix glycoprotein (M), and a nucleocapsid protein (N). In this article, we address the structure of the transmembrane domain of the SARS-CoV E protein in a model phospholipid membrane by x-ray scattering.

S, M, and N proteins of different coronaviruses have been broadly studied for their important roles in receptor binding and virion budding. The significance of the E protein has been realized only much more recently (8). This membrane-bound constituent of the virion was not immediately recognized as a viral structural protein, owing to its small size (~10 kDa) and its very low abundance relative to the M, N, and S proteins. Today, coronavirus E proteins are known to play an important role in viral morphogenesis. Coexpression of mouse hepatitis virus (MHV) E and M proteins results in the production of virus-like particles (9,10), indicating that neither the nucleocapsid nor the viral spike are needed for viral budding. The interaction between the two proteins relevant for the budding process is thought to take place in pre-Golgi compartments whereby the cytoplasmic domains of the two proteins interact (11). During the expression of E protein the Golgi apparatus changes its morphology dramatically (12), explaining in part E protein's ability to induce apoptosis (13,14). Expression of M protein from several coronaviruses on its own did not produce virus-like particles (9,10,15–17). On the contrary, expression of MHV E protein on its own caused the release of vesicles containing E protein, highlighting the important role of this small protein. This pattern seems to be a general result for coronaviridea (15,16).

E proteins are well conserved within each of the different groups of coronaviruses (18). Regarding the sequence, it is possible to make the following generalization for all E proteins: E proteins are all small proteins (~75 residues) with an unusually long hydrophobic stretch (25–30 amino acids), placed in between a hydrophilic N- and C-terminus, ~8 and ~40 residues long, respectively. Note that the length of the hydrophobic segment of E proteins is significantly larger than the average length of a transmembrane α-helix, which is only ~21 residues (19). The SARS-CoV E (SARS-CoV E) protein is a 76-residue (NH_3^+-MYSFVS**EETG-TLIVNSVLLFLAFVVFLL VTLAILTALR**LCAYCCNI-VNVSLVKPTVYVYSRVKNLNSSEGVPDLLV-COO^-) polypeptide. The region in bold type in the sequence represents the hydrophobic transmembrane domain (TMD) of the protein.

In this article, we investigate the structure of dimyristoylphosphatidylcholine (DMPC) bilayers with reconstituted TMD of SARS-CoV E by x-ray reflectivity and grazing incidence scattering, as a function of peptide/lipid molar ratio *P/L* and the hydration level of the headgroups. Peptides were synthesized that encompassed the entire hydrophobic region of the protein (Glu-7 to Arg-38), as depicted in Fig. 1 *a*. In a previous study, we focused on the secondary structure of TMD using Fourier transform infrared (FTIR) spectroscopy, x-ray reflectivity, and molecular modeling (20). FTIR dichroism on oriented bilayers showed a highly helical backbone structure oriented perpendicular to the bilayer. At the same time, x-ray reflectivity analysis comparing an unlabeled peptide and a peptide labeled with iodine at position Phe-23 in the center of the hydrophobic stretch allowed us to pinpoint the location of the central Phe-23

Submitted August 23, 2005, and accepted for publication November 21, 2005.
Address reprint requests to T. Salditt, Institute for X-ray Physics, University of Göttingen, Friedrich-Hund-Platz 1, D-37077 Göttingen, Germany. Tel.: 49-551-399427; Fax: 49-551-399430; E-mail: tsaldit@gwdg.de.

0006-3495/06/03/2038/13 $2.00
doi: 10.1529/biophysj.105.072892

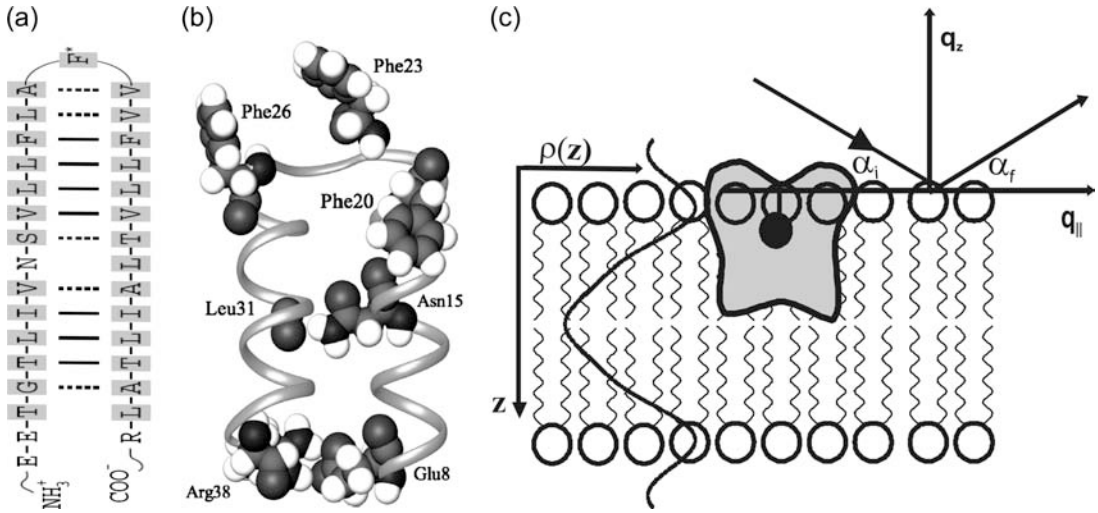

FIGURE 1 (*a*) Ribbon diagram of the structural model derived from the TMD of SARS-CoV E protein taken from Arbely et al. (20). (*b*) The sequence diagram of the SARS-CoV E protein around a pseudo point of symmetry (i.e., Phe-23) as two short helices forming the hairpin model. (*c*) Sketch illustrating a bilayer with incoming and reflecting beams in a reflectivity setup. α_i and α_f denote the angles between the sample surface and the incoming and reflected beams, respectively. q_z denotes the momentum transfer in the *z*-direction, and $q_{||}$ the lateral momentum transfer. Also shown is a schematic of the SARS-CoV E protein embedded in the membrane bilayer. The dot represents the iodinated Phe-23 group.

group in the bilayer electron-density profile. It was found to be located at a position displaced ~16–17 Å from the bilayer center in the headgroup region. Here we give a more complete account of these experiments, complemented by additional results obtained at a wider range of *P/L*, and also for three different levels of hydration. Furthermore, we investigated changes in the acyl-chain ordering at high protein concentrations. Finally, anomalous x-ray reflectivity was used to verify the location of the iodine label.

Concluding from previous FTIR and x-ray results (20) for high *P/L* samples, a short hairpin conformation inserted perpendicular to the plane of the membrane was postulated for the sequence (see Fig. 1 *b*). The hairpin forms an inversion about a pseudocenter of symmetry (see Fig. 1 *b*) . Molecular modeling supported the model and showed that the two helices are likely to be stabilized by specific bonds, namely a salt bridge between Glu-8 and Arg-38, and a hydrogen bond between a single asparagine amino acid in the two helices and the backbone amide group (see Fig. 1 *a*). An alternative model had been proposed by Shen and coworkers for the SARS-CoV E protein (21), based on CD spectra taken in aqueous solution. According to this model, the SARS-CoV E protein sequence forms a single transmembrane (TM) helix, and a short β-sheet segment forming a hydrogen bond with the lipid bilayer. This model cannot be reconciled with a Phe-23 position displaced from the bilayer center. It would also lead to a significant hydrophobic mismatch between hydrophobic amino acids and acyl chain thickness, since the average number of amino acids in a transmembrane helix needed to span the entire bilayer is only ~21. Furthermore, recent antibody binding results with an epitope-tagged MHV E protein are indicative of the protein traversing the lipid bilayer twice, whereby both termini of the protein reside in the virus lumen (22). This can well be understood, if the hairpin conformation is the general motif of E proteins. On the other hand, molecular dynamics simulation has been used recently as a test for evolutionary conservation using several coronavirus protein homologous sequences, and points to a transmembrane oligomer topology (23). Note that the x-ray study alone is not able to prove or disprove the hairpin conformation. However, it can provide important structural constraints, as well as the electron-density profile of the lipid bilayer as a function of *P/L* (see Fig. 1 *c*).

This introduction is followed by the sections Materials and Methods, X-ray Reflectivity and Electron-Density Profiles, Anomalous Reflectivity, and Acyl Chain Ordering Induced by E Protein. Finally, the article closes with Summary and Conclusions.

MATERIALS AND METHODS

Materials

Dimyristoyl-*sn*-glycero-3-phosphatidylcholine was purchased from Avanti Polar lipids (Alabaster, AL). The purity of DMPC is claimed to be 99%. Therefore the lipid was used without further purifications. Chloroform (Chl) and 1,1,1,3,3,3-hexafluor-2-propanol (HFI) (purity 99.8%) were purchased from Sigma (Schnelldorf, Germany).

Peptide synthesis

The peptide was synthesized and purified (residues 7–38) by standard solid-phase *N*-(9-fluorenyl) methoxycarbonyl (Fmoc) chemistry as described in Arbely et al. (20). Two different synthetic peptides were made: an unlabeled peptide and one that contains iodine at position 23 (i.e., phenylalanine) of the sequence.

Preparation of lipid-protein multilamellar stacks

Lipids were used as purchased to prepare multilamellar bilayers of DMPC/protein complexes following the procedure described by Seul and Sammon (24). The lipids were first dissolved in a solution of Chl/HFI (1:1, v/v) at a concentration of 20 mg/ml, whereas the proteins were dissolved in a solution of Chl/HFI (40:60%, v/v) at 2 mg/ml since the protein is more soluble at higher HFI concentrations. Varied amounts of the protein stock solution were then mixed with the DMPC stock solution at a final concentration of 5 mg/ml, which yields the desired *P/L* ratio. Pure solvents were added to yield an identical final lipid concentration. The protein/lipid ratio *P/L* ranged from 1/500 to 1/7.5. The mixed solutions were spread on Silicon substrates, cleaned by two 15-min cycles of ultrasonic bath in methanol, followed by two 15-min cycles in ultrapure water (18 MΩ cm, Millipore, Bedford, MA), and finally dried under a nitrogen stream. A droplet of 200 μl was then spread on the *Si*-wafer of typically 15×25 mm^2 positioned in an exactly horizontal plane. The spread solution was allowed to dry very slowly to prevent film rupture and dewetting. The samples were then exposed to high vacuum for 12 h to remove completely all the solvent traces. Afterward, the samples were rehydrated, yielding film thicknesses in the range of $D \simeq 2 - 5\mu m$. Such a procedure produces multilamellar stacks well aligned with respect to the substrate, with a typical mosaicity (orientational distribution) less than the instrumental resolution (i.e., 0.01°) (25). A very low mosaicity is a prerequisite in applying interface-sensitive x-ray scattering techniques for structural studies of solid-supported bilayers. To examine the sample quality, we used light microscopy in bright-field contrast (Olympus, Melville, NY; objective, Neofluar 10×/0.3) to image the samples after the deposition at different *P/L*. The samples were kept in the fluid state at the same temperature as for the x-ray experiments. A significant effect of the concentration of the SCoV E protein on the morphology of the supported membranes was observed. Images recorded in the L_α state at temperature $T = 45°$ and relative humidity $R.H. = 98\%$ are shown in Fig. 2. The samples were kept in a sealed temperature-controlled chamber (Julabo, Seelbach, Germany) with a water reservoir at the bottom for hydration. Note that multilamellar films are known to exhibit a pronounced domain structure with a large variation in local film thickness. At the same time, the orientation of the bilayers is almost perfect, despite the limited lateral extension of the domains, leading to a patch-like morphology (see Fig. 2 *a* for the case of pure DMPC).

A significant change in the domain size and texture is observed already at a relatively small concentration of SARS-CoV E protein. At $P/L = 0.002$, the formation of small irregularly shaped domains, which comprise a significant fraction of the bilayer surface area, are observed instead of the relatively large domain structures in pure DMPC films (see Fig. 2 *b*). This defect structure is interconnected, and, as the concentration is increased to $P/L = 0.01$, changes to a pattern with even smaller domains. The typical length scales of the defect structures remain small for $P/L = 0.01$ and 0.02 (Fig. 2, *c* and *d*), until at higher concentrations (i.e., 0.05 and 0.10) it increases again. The pattern at $P/L = 0.05$ exhibits many individual structures that are not connected (Fig. 2 *e*). Finally, a star-like morphology with relatively large smooth areas evolves on the top of the lipid film (Fig. 2 *f*). These changes are very reproducible for different samples and upon translation of the illuminated spot on the sample. The results show that in the L_α phase, the SARS-CoV E protein drastically affects the multilayer morphology, possibly by changing the line tension between the domains.

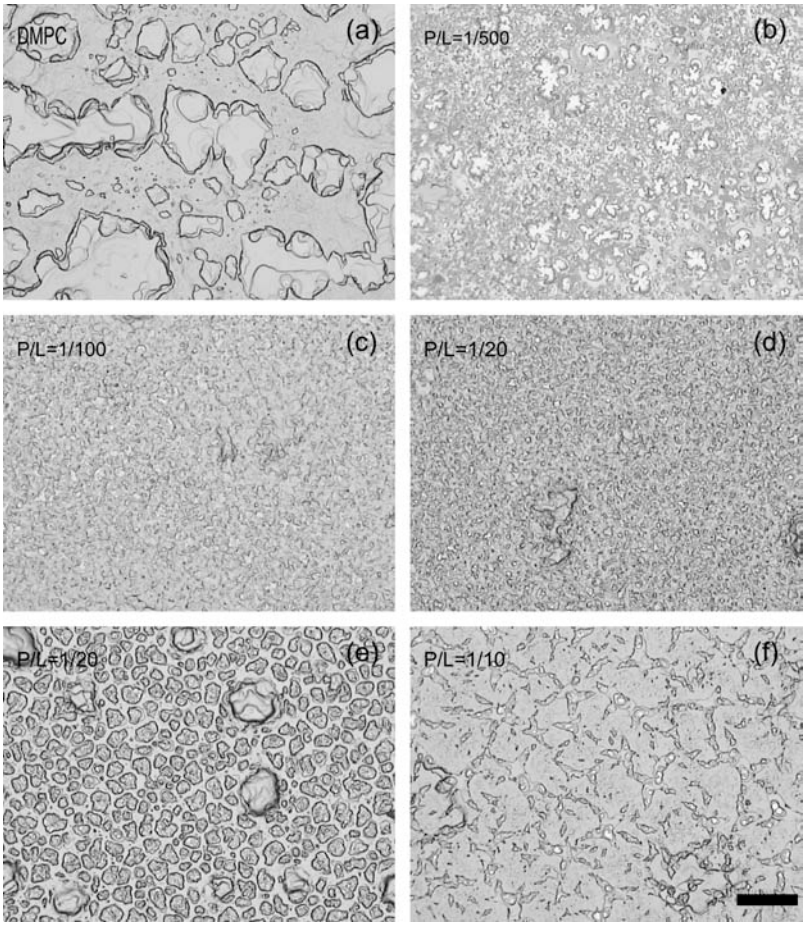

FIGURE 2 L_α-phase (i.e., $T = 45°$C and $R.H. = 98\%$) protein/lipid film images by bright-field contrast for different protein concentrations *P/L*. The defect structures and domain sizes change with *P/L*. Scale bar, 100 μm.

X-ray reflectivity

Before x-ray reflectivity measurements, the resulting multilamellar stacks were inserted in a closed temperature- and humidity-controlled chamber. The chamber consists of two concentric stainless steel cylinders, with kapton windows. The chamber temperature was maintained by a flow of oil connected to a temperature-controlled reservoir (Julabo). The temperature was measured close to the sample holder using a Pt100 sensor with thermal stability in the range of 0.02 K over several hours (26). The average temperature of the samples was kept at $T = 45°C$, well above that of the chain-melting transition. The samples were mounted in the inner cylinder of the chamber facing a humid atmosphere controlled by adding a salt to a water reservoir placed at the bottom of the cylinder (27). By changing the salt type one can vary the relative humidity from 11% to 100%. We used three types of salt, namely LiCl, NaCl, and K_2SO_4, leading to $R.H. = 11\%$, 75%, and 98%, respectively. When using K_2SO_4, DMPC bilayers were typically swollen up to a repeat distance of $d \simeq 50$ Å in the L_α-phase. At both $R.H. = 75\%$ and $R.H. = 98\%$, the membranes were in the fluid L_α state, whereas the $R.H. = 11\%$ curves were indicative of a gel phase.

The reflectivity experiments were carried out on the bending magnet beamline *D*4 of the DORIS storage ring at the synchrotron radiation laboratory HASYLAB/DESY (Hamburg, Germany) using a photon energy of 11 keV (i.e., $\lambda = 1.13$ Å), set by a Si(111) monochromator. The chamber was mounted on the *z*-axis diffractometer with the samples oriented vertically. The reflectivity curves were measured with a fast scintillation counter (Cyberstar, Oxford Instruments, Eynsham, U.K.) using motorized collimating slits on both incident and reflected beam paths. The reflectivity curves were corrected for ring current, sample illumination, and diffuse background (offset-scan).

In the following text, we briefly repeat the principles of x-ray reflectivity and the Fourier synthesis (FS) method as tools to determine the electron density of the protein-lipid system (28). To record a reflectivity curve, the incident beam with wave vector k_i has to be collimated to less than a few hundredths of a degree and directed on the sample at glancing incidence angle α_i. The reflected intensity is then measured as a function of α_i under specular conditions (e.g., at an exit angle $\alpha_f = \alpha_i$), with the wave vector of the exit beam denoted by k_f. Thus, the momentum transfer of the elastic scattering $q = k_f - k_i$ is always along q_z, with the *z* axis parallel to the sample normal (Fig. 1). Typically, the reflectivity can be recorded over seven to eight orders of magnitude (after correction for diffuse scattering and background), as measured in a so-called offset scan. To this end, the x-ray reflectivity in the semikinematic approximation from an interface characterized by electron-density profile $\rho(z)$ between two media of electron densities ρ_1 and ρ_2 is given by Braslau et al. (29)

$$R(q_z) = R_F(q_z)\left|\Phi(q_z)\right|^2 = R_F(q_z)\left|\frac{1}{\Delta\rho_{12}}\int\frac{\partial\rho(z)}{\partial z}e^{iq_z z}dz\right|^2, \tag{1}$$

where R_F is the Fresnel reflectivity of the ideal (sharp) interface between the two media, q_z is the scattering vector, and $\Delta\rho_{12}$ is the density contrast of the two mediums. In this formalism the interface normal is along the *z* axis and $\rho(z)$ is the laterally averaged electron density. For the moment we ignore the effect of absorption, which can be accounted for by introducing an imaginary component of the wave vector. Then, the function $R_F(q_z)$ can be written in terms of the critical momentum transfer q_c as $|q_z - q'_z|/|q_z + q'_z|$ with $q'^2_z = |q_z^2 - q_c^2|$. The critical momentum transfer or the critical angle is directly related to the density contrast between the two media by $q_c = 4\pi/\lambda\sin(\alpha_c) \cong 4\sqrt{\pi r_0 \Delta\rho_{12}}$, with r_0 denoting the classical electron radius. In this case, medium 1 corresponds to air and medium 2 corresponds to the solid substrate (i.e., silicon). The multilamellar stack of bilayers is modeled by an interface with a partially oscillatory density profile as described in Salditt et al. (28). Using the linearity of the integrand in Eq. 1, one can decompose it into parts, the first one accounting for the density increment at the substrate that does not depend on the multilamellar bilayers, and a second one that contains entirely the information about the bilayer stack. The second term can be broken up into two parts: the form factor $f(q_z)$ and the structure factor $s(q_z)$. The structure factor contains the parameters of the multilamellar stack. For an ideal one-dimensional stacking, $s(q_z)$ would be simply given by

$$s(q_z) = \sum_{n=1}^{N_0} e^{i(nq_z d)}, \tag{2}$$

where *d* is the periodicity and *N* is the total number of layers in the stack. The form factor, which characterizes the electron-density distribution, is defined in this context as

$$f(q_z) = \int_{-d/2}^{d/2}\frac{\partial\rho(z)}{\partial z}e^{iq_z z}dz. \tag{3}$$

The electron-density profile of the bilayer can be defined in various ways. A practical parameterization is in terms of its Fourier coefficients, since the number of parameters can easily be adapted to the resolution of a particular experiment. The deviations from the average bilayer electron density ρ_0 in terms of the first N_0 Fourier coefficients f_n can thus be written as

$$\rho(z) = \sum_{n=1}^{N_0}\nu_n f_n \cos\left(\frac{2\pi nz}{d}\right), \tag{4}$$

where the phases $\nu_n = \pm 1$ are reduced to positive/negative signs due to the mirror plane symmetry of the bilayer. In general, an educated guess of the phasing can be deduced from the basic bilayer profile or the data as discussed in Salditt et al. (28). The coefficients f_n can be related to the integrated intensities under the reflectivity curve after application of (Lorentz) correction factors, e.g., q_z^{-1} or q_z^{-2}. For highly oriented films, a correction factor of q_z^{-1} has been proposed in Tristram-Nagle et al. (30) and Gandhavadi et al. (31). However, in the absence of a rigorous derivation it remains unclear in which approximation a simple factor suffices to correct the raw data. It is clear that effects of mosaicity, absorption, and Fresnel reflectivity terms all influence the intensities of the Bragg peaks, leaving aside for the moment additional effects of the structure factor, e.g., due to thermal fluctuations. In Li et al. (32), an experimental approach is used to address these questions, where the profiles derived from full q_z range fitting are compared to those computed by the FS method, with different correction factors. Here we use $f_n \propto \sqrt{nI_n}$, which can be regarded as an approximation. Using a more rigorous reflectivity analysis it was found that the approximation is quite good, in particular for the bilayer thickness, which is of importance here. Furthermore, a comparison of profiles for labeled and unlabeled proteins should be meaningful even if systematic errors persist in the profile resulting from the approximation in this data treatment. Finally, the electron density of the bilayer lipid membrane on an arbitrary scale (no absolute units) has been calculated form the measured peak intensities as

$$\rho(z) = \sum_{n=1}^{N_0}\sqrt{nI_n}\nu_n \cos\left(\frac{2\pi nz}{d}\right). \tag{5}$$

RESULTS AND DISCUSSION

X-ray reflectivity and electron-density profiles

Characteristic reflectivity curves of the noniodinated sequence *P/L* series are shown in Fig. 3, shifted vertically for clarity, for three different swelling states (R.H.). Similar reflectivity curves were obtained for the analogous series with the iodinated sequence. The reflectivity is plotted as a function of the vertical momentum transfer q_z after subtraction of the diffuse scattering (offset scan), and after

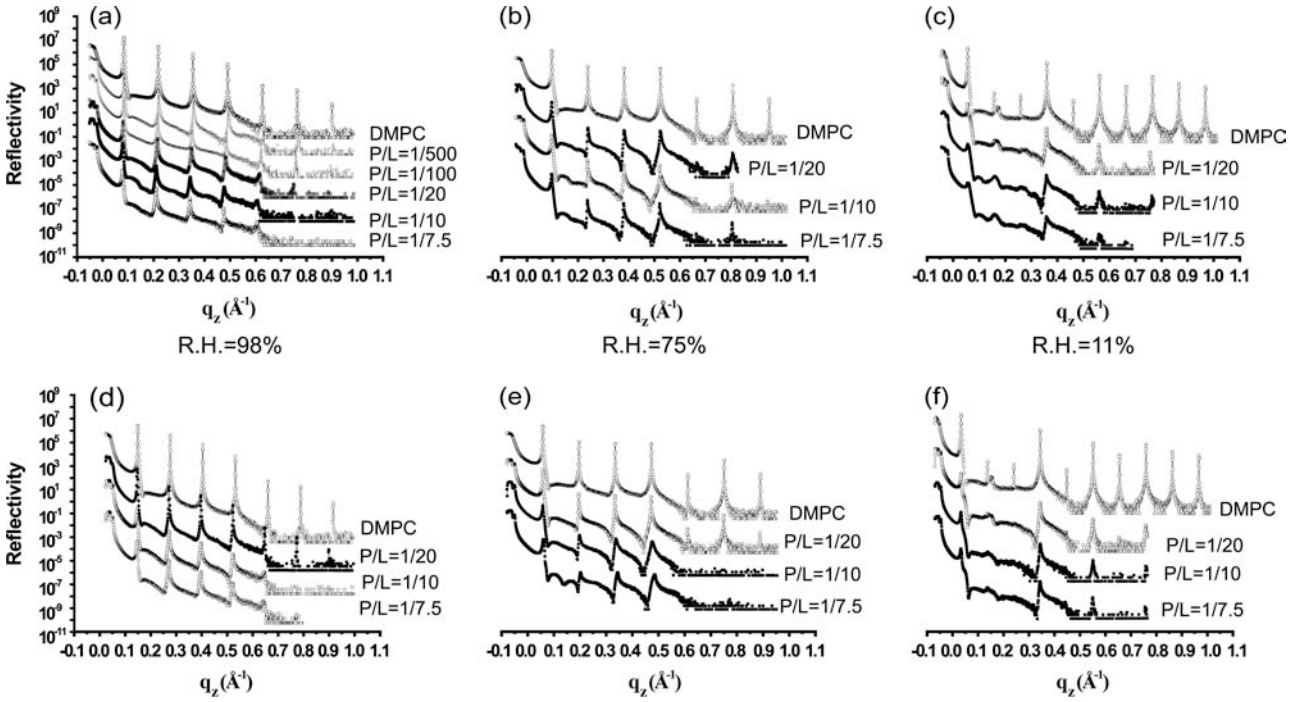

FIGURE 3 Reflectivity curves of multilamellar DMPC/SARS-CoV E protein membranes at three distinct *R.H.* and constant $T = 45°C$. Different *P/L* ratios are presented for the noniodinated (*upper panels*) and iodinated (*lower panels*) SARS-CoV E protein. The curves are shifted vertically for clarity. The curves exhibit the typical pattern of a lamellar structure with well defined periodicities *d* and large vertical domain sizes as evidenced from the sharp peaks. The smaller peak heights for $P/L = 1/10$ reflect the increase of fluctuations and/or static disorder with *P/L*. All data has been corrected for illumination, diffuse background, and beam monitor.

illumination correction. The curves show the typical features of highly oriented multilamellar films: the plateau of total reflection at small q_z, and a set of sharp and intense equidistant Bragg peaks. The intensity and number of Bragg peaks decreases with *P/L*, indicative of peptide-induced lamellar disorder. The complete *P/L* series was measured at constant temperature $T = 45°C$, but at different swelling states, controlled by hydration from saturated salt solutions (see Materials and Methods), corresponding to nominal relative humidities of 98%, 75%, and 11%. The first two R.H. values correspond to the L_α phase where the Bragg-peak intensities decay more homogenously.

The gel-phase curves show a particularly interesting pattern upon addition of the protein, where odd reflection orders with the exception of $n = 1$ are significantly suppressed, but since we are more interested in the fluid state, we leave these curves aside for the moment. In the fluid state, the reflectivity curves depend in a systematic way on the peptide concentration. This dependency and the corresponding *d*-spacings are identical for the iodinated and noniodinated series, indicating that the presence of the label does not perturb the system.

To evaluate the data, we used the Fourier synthesis method, using solely the integrated peak intensities to compute the density profile, rather than full q_z range fits of the curves (28), as discussed in the previous section. The latter has a much larger potential for structural analysis and yields density profiles in absolute units, but is also very time-consuming and more difficult to achieve. Although we are working toward this goal, we are not yet in possession of a comprehensive reflectivity fitting model and software for these films. A suitable model function must take into account effects of absorption, thermal fluctuations, static defects, and instrumental resolution, and yet keep the number of parameters manageable. Therefore we turn here to the Fourier synthesis method, which is commonly used in the literature but which poses some serious problems, as discussed in Li (33). In particular, Fresnel-type reflectivity curves are not included in this simplified approach. Moreover, changes in the structure factor with *P/L* are falsely attributed to the form factor, since the structure factor is tacitly assumed to be that of the ideal lattice. More than seven lamellar reflectivity reflections were observed for the peptide-free bilayers, whereas only five or four orders persist in the presence of the peptide sequence, independent of iodination. This phenomenon is typical for many membrane active peptides or proteins and leads to a smoothing of the deduced bilayer profile. Of course, the local profile is not necessarily flatter for high *P/L*. Instead, this effect probably results from the increased lamellar disorder, since the determined profiles have to be regarded not as intrinsic profiles, but rather as convolutions of the intrinsic profiles with the distribution function of the bilayer position, which broadens with increasing lamellar disorder. Five orders of reflectivity data are clearly enough to

calculate the electron distribution of the peptide/bilayer with a sufficiently high resolution to determine structural quantities, as the distance between the headgroups, e.g., the distance between the two maxima corresponding to the phosphorus atoms d_{pp}. A summary of the integrated peak intensities for 98%, 75%, and 11% R.H. are presented in Table 1.

The centrosymmetric electron-density profiles of the bilayers containing noniodinated and iodinated SARS-CoV E protein obtained at $R.H. = 98\%$ for different P/L are shown in Fig. 4, on an arbitrary scale. The profiles were calculated using Eq. 6, with appropriate choice of phases (−, −, +, −, +, −, −). The curves have been normalized such that the area under the first Bragg peak is set to be 1, whereas the higher-order Bragg peaks were properly scaled with respect to the first peak intensity. Similar curves were obtained at 75% and 11% R.H. The well known interpretation of the profiles is as follows: the two mean peaks of $\rho(z)$ on either side of the figure correspond to phospholipid headgroups, the two side minima to the water layer, and the central minimum to the terminal methyl moiety of the hydrocarbon chains.

The bilayer d-spacing and thickness d_{pp} are shown in Fig. 5 as a function of P/L and at different hydration pressures. For all P/L samples at the two different $R.H.$ values in the fluid state, d was obtained from the reflectivity curves by fitting the q_z values at each Bragg peak as a function of Bragg order (i.e., n) to a straight line. The presence of peptides in the lipid induces a shift in Bragg peaks toward smaller q_z values as compared to the pure lipid. Labeling the peptide with iodine did not change the d-spacing significantly. At fixed P/L ratio, the lamellar repeat distance decreases with increasing osmotic pressure, reflecting the decrease in water layer thickness. The solid lines correspond to third-order polynomial fits, which are simply guides to the eye and do not represent any theoretical model. At 98% R.H., the d-spacing increases as a function of P/L, whereas at 75% R.H. the lamellar spacing is approximately constant for $P/L < 1/10$. Above this value a small difference in d-spacing between the iodinated and the noniodinated samples (i.e., <1 Å) is observed.

The bilayer thickness defined as the distance between the two maxima associated with the phosphorus group d_{pp} as a function of P/L was determined from $\rho(z)$. Note that, d_{pp} is unaffected by the normalization of the electron-density profiles (34). The two different R.H. series in the fluid state are presented in Fig. 5 *b*. An increase in d_{pp} is observed for all SARS-CoV E protein concentrations in the bilayer for both R.H. series. Only at high P/L and for $R.H. = 98\%$ is there a significant effect of the iodine label. For the other

TABLE 1 Summary of experimental results for x-ray reflectivity measurements on DMPC mutilamellar bilayer containing iodinated and noniodinated SCoV E protein

Hydration condition*		P/L†									
$R.H. = 98\%$	DMPC	1/500		1/100		1/20		1/10		1/7.5	
Integrated intensity†		I	Non-I	I	Non-I	I	Non-I	I	Non-I	I	Non-I
I_0	1	–	1	–	1	1	1	1	1	1	1
I_1	1.39E-1	–	4.76E-2	–	4.7E-2	4.65E-2	4.45E-2	3.0E-2	1.64E-2	5.0E-2	2.6E-2
I_2	2.80E-2	–	1.37E-2	–	0.81E-2	1.15E-2	6.0E-3	5.2E-3	2.15E-3	9.1E-3	3.5E-3
I_3	4.0E-3	–	3.43E-3	–	1.05E-3	2.41E-3	1.0E-3	8.8E-4	3.7E-4	1.3E-3	4.9E-4
I_4	8.0E-5	–	1.7E-5	–	5.86E-5	16.0E-5	6.9E-5	5.6E-5	2.6E-5	7.6E-5	3.7E-5
I_5	3.30E-5	–	5.4E-5	–	1.18E-5	0	0	0	0	0	0
I_6	0	–	0	–	0	0	0	0	0	0	0
$R.H. = 75\%$											
I_0	1	–	–	–	–	1	1	1	1	1	1
I_1	3.29E-2	–	–	–	–	7.1E-3	5.5E-3	2.4E-3	4.2E-3	9.5E-4	2.9E-3
I_2	1.89E-2	–	–	–	–	4.6E-3	3.5E-3	2.0E-3	1.8E-3	1.4E-3	1.7E-3
I_3	1.8E-2	–	–	–	–	4.2E-3	3.6E-3	1.5E-3	1.6E-3	1.3E-3	1.6E-3
I_4	3.35E-5	–	–	–	–	5.3E-6	3.2E-6	0	0	0	0
I_5	6.98E-4	–	–	–	–	9.5E-5	4.3E-5	0	2.6E-5	0	3.2E-5
I_6	3.63E-4	–	–	–	–	1.7E-6	0	0	0	0	0
$R.H. = 11\%$											
I_0	1	–	–	–	–	1	1	1	1	1	1
I_1	1.43E-4	–	–	–	–	4.9E-3	4.9E-3	5.1E-4	3.4E-3	3.9E-4	2.4E-3
I_2	17.64E-5	–	–	–	–	0	1.9E-3	0	3.1E-3	0	2.7E-3
I_3	4.78E-2	–	–	–	–	5.2E-3	8.3E-3	2.9E-3	1.3E-3	2.9E-3	5.1E-4
I_4	3.20E-5	–	–	–	–	0	0	0	0	0	0
I_5	4.48E-4	–	–	–	–	2.4E-4	4.3E-5	6.5E-5	6.3E-5	1.3E-4	2.0E-5
I_6	6.7E-6	–	–	–	–	0	0	0	0	0	0

P/L indicates the protein/lipid ratio, and is given for iodinated (I) and noniodinated (Non-I) samples.

*Samples hydrated through vapor by equilibration with saturated salt solutions indicated by $R.H.$ value.

†The integrated intensities under each Bragg peak of the reflectivity curve. All the peaks were normalized with respect to the first Bragg peak in the reflectivity curve. See text for further explanation.

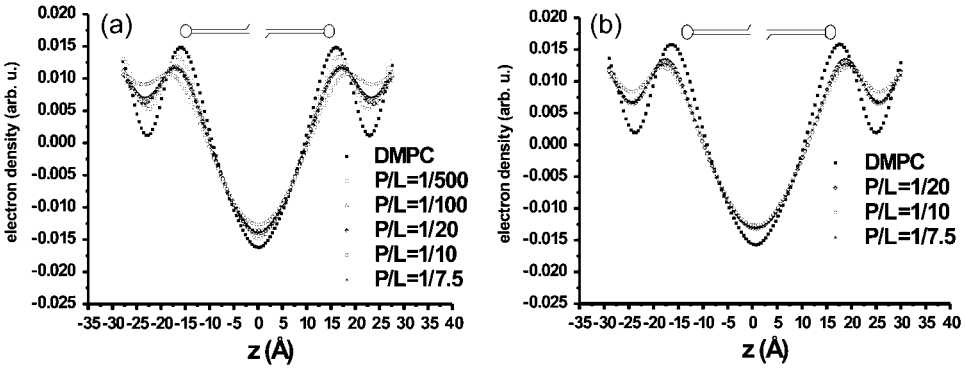

FIGURE 4 The electron density profiles of the pure DMPC bilayer and different *P/L* ratios of unlabeled (*a*) and labeled (*b*) SARS-CoV E protein. The curves were computed from the integrated peak intensities taken from Fig. 3 (i.e., *R.H.* = 98%) by the FS method. The normalization procedure is described in the text.

samples, the labeling does not change the structural parameters. For each hydration value, the two data sets (i.e., labeled and unlabeled) were fitted to a third-order polynomial, which again serves as a guide to the eye. With increasing osmotic pressure the bilayer becomes slightly thicker. This phenomenon is well known for pure lipid bilayers and corresponds to bilayer thickening upon dehydration. The effect of bilayer thickening with *P/L* is in striking contrast to the bilayer thinning observed for many α-helical amphiphilic peptides, which have created some interest recently due to antibiotic activity. For this class of peptides, bilayer thinning drives the transmembrane insertion. Above a critical concentration $(P/L)^*$, there is a transition from a parallel to a perpendicular (transmembrane) conformation (35–37).

Finally, the electron-density curves of labeled and unlabeled protein are compared for constant *P/L* and *R.H.* to determine the position of the labeled group in the lipid bilayer (Fig. 6). The result supports the helical hairpin model, as put forward previously on the basis of a limited x-ray data set in combination with FTIR results (20). Fig. 6 shows the electron-density profile at $P/L = 1/10$ and 1/7.5 for the labeled and unlabeled peptide at $R.H = 98\%$ and 75%. The labeled and unlabeled curves were compared as follows. The Bragg peak intensities of both curves were normalized to the first Bragg peak of the unlabeled sample. The profiles were then computed by Fourier synthesis, the zero-density value corresponding to the mean density. Finally, the two curves were multiplied by the same scalar so that the maximum in the headgroup region of the iodinated electron-density curve is 1.

At high mol % of the iodine, the electron-density difference is large enough to locate the position of the iodine (or the phenylalanine) with respect to the bilayer center. Examining the profiles in Fig. 6, *a* and *b*, reveals a small increase of electron density in the headgroup region of the bilayer in the presence of the iodine label. In the central region of the lipid-peptide profile, corresponding to the bilayer hydrophobic core, the changes caused by iodine are small and below the experimental accuracy. Subtracting the electron-density profiles of lipid bilayers containing iodinated and unlabeled SARS-CoV E proteins should result in an effective iodine-density profile. Maxima in these profiles can then be used to determine the iodine position (z_i) from the bilayer center. At higher hydration the pronounced maxima in these curves indicate the most probable position of the iodine at $z_i = 16.5$ and 16.6 Å for $P/L = 1/10$ and 1/7.5, respectively. This implies that the iodine-labeled phenylalanine is located adjacent to the headgroup region. The iodine electronic distribution at 75% R.H. (see Fig. 6, *c* and *d*) shows a different behavior. The oscillatory profile with its small amplitude suggests a more disordered state. A small increase in its density profile outside the headgroup region could suggest that the protein partly aggregates between the bilayers, but it is unclear whether this small maximum is really significant.

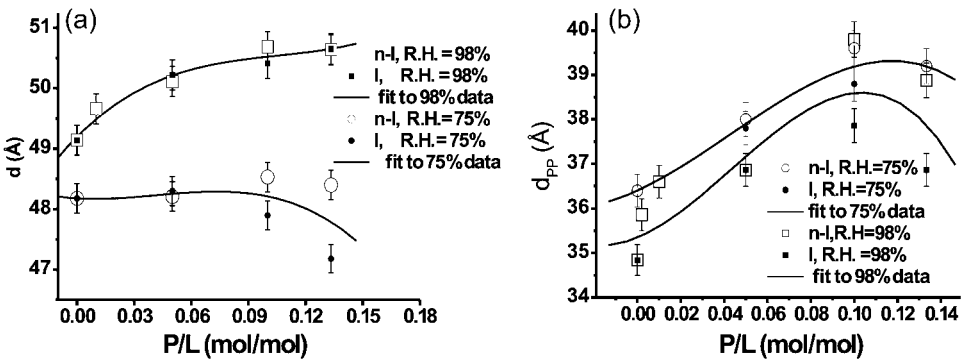

FIGURE 5 (*a*) The membrane repeat distance *d* as a function of *P/L* for SARS-CoV E protein at $T = 45°C$ and two different *R.H.* (*b*) The bilayer thickness d_{pp}, defined as the peak-to-peak distance in the electron-density profiles. The iodinated samples are indicated by solid symbols.

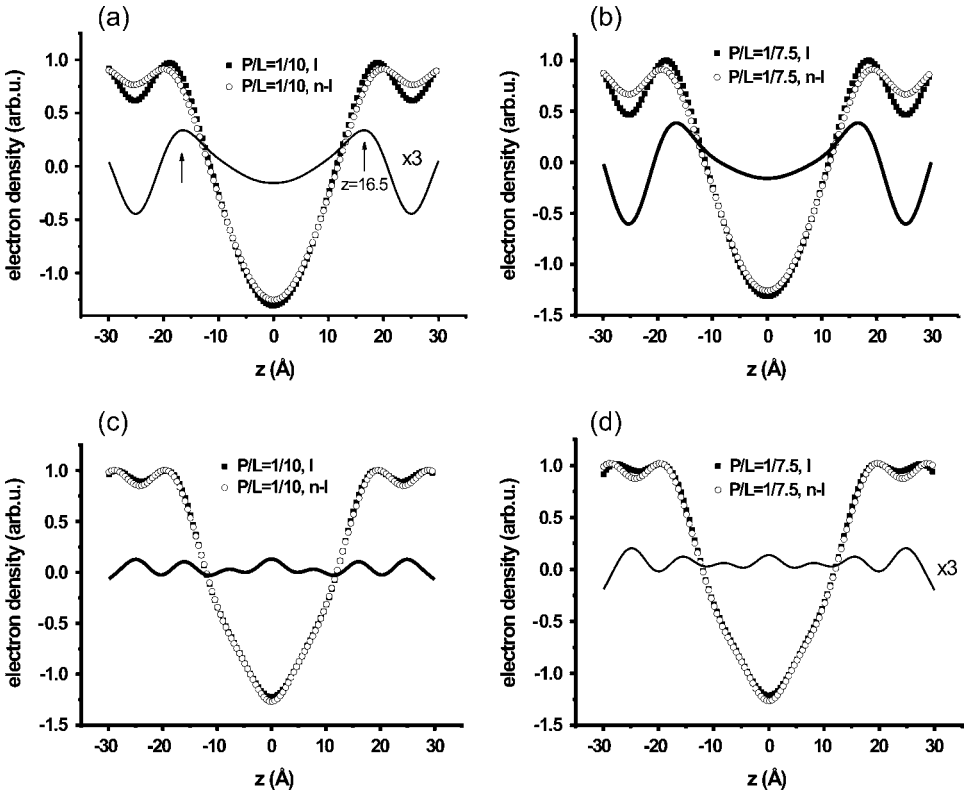

FIGURE 6 (*a* and *b*) Electron-density profiles of the *P/L*: 1/10 and 1/7.5, respectively, of the iodinated and noniodinated SARS-CoV E protein at $R.H. = 98\%$ in arbitrary units. The electron-density profiles were normalized with respect to the first integrated peak of the labeled curve. The iodine-density profile (the lower curve in the panel) was calculated by subtracting the electron densities of the noniodinated from the curve of the iodinated SARS-CoV E protein. The difference curve depicted in the figure has been multiplied by a factor of 3, and the arrows indicate the position of the iodine label adjacent to the headgroups. (*c* and *d*) The same profiles as in *a* and *b* but at $R.H. = 75\%$. The position of iodine is not well defined in this case.

Anomalous reflectivity

The above results were solidified by performing an anomalous x-ray reflectivity study (AXR) on the same samples. Here, we briefly describe the experimental procedure and give a comparison between both sets of results. The experimental details were given in a previous article (38). The experiment was performed at the European Synchrotron Radiation Facility/ID1 (Grenoble, France) by choosing the incoming x-ray energy in the vicinity of the L_{III} adsorption edge (i.e., $E_L = 4.5545$ keV) of the iodine. The anomalous effect at the iodine adsorption edge is then used to determine the label position within the lipid bilayer. Two samples at $T = 45°C$ and $R.H. = 98\%$ were used in the experiment: pure DMPC and $P/L = 1/10$ with iodinated Phe-23. Reflectivity curves were measured at five different energies (4.3975 keV $< E <$ 4.5675 keV) on both samples. AXR was first performed on the pure DMPC sample under the same instrumental and environmental conditions as a test experiment and to check for x-ray radiation damage. In fact, no severe damage to the sample was observed despite the relatively high absorption coefficient at these photon energies. Next, the sample with protein was measured at the same five energies. As before, all reflectivity and rocking curves indicate a highly organized multilamellar film on solid supports. For DMPC, more than seven lamellar reflectivity peaks of reflection were obtained, whereas only four to five orders of reflection were observed in the presence of SARS-CoV E protein due to lamellar disorder and fluctuations (data not shown). After plotting the curves against q_z the differences can be attributed exclusively to the anomalous effect, assuming that the sample state remains the same over the course of the experiment (several hours). Next, all peaks of the reflectivity curves are analyzed by the FS method to obtain the electron-density profiles $\rho(z, E)$ for all energies as described in Materials and Methods. The iodine-density profile was calculated from the differences in the electron-density profiles, e.g., $\Delta\rho_I(z, E) = \rho_E(z) - \rho_{E_L}(z)$ (Fig. 7). In line with the previous results, the maximum in the iodine difference curves is found to be in the headgroup region at 18.1 Å from the center of the lipid bilayer (Fig. 7, *arrows*). However, the density difference curves taken at different photon energies agree only qualitatively and do not follow the quantitative scaling of the atomic form factor, as has been tentatively ascribed to systematic errors in the experiment (in particular sample drift in temperature or humidity) (38).

Effect of peptide concentration on chain ordering

The effect of adding SARS-CoV E protein to lipid bilayers leads to changes not only in the bilayer electron-density profile, but also in the short-range ordering of acyl chains. Although in most cases adsorbed or inserted peptides and proteins further reduce the correlations in the fluid phase, leading to a decrease and broadening of the chain correlation peak, SARS-CoV seems to have the opposite effect (Fig. 8). The scattering distribution as measured in grazing incidence

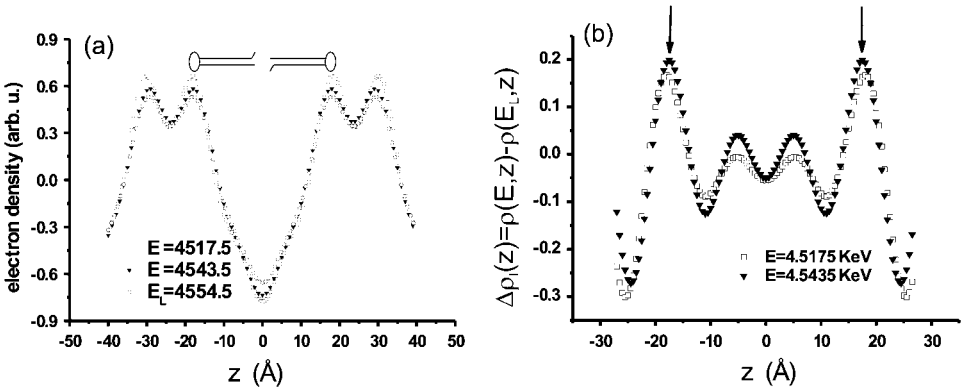

FIGURE 7 (*a*) Electron-density profiles obtained by AXR as calculated from the FS method at three energies at $R.H. = 98\%$ and $T = 45°C$. (*b*) Electron-density profile difference, e.g., $\Delta\rho_I(z,E) = \rho_E(z) - \rho_{E_L}(z)$. The iodine position is indicated by the arrows and is in agreement with the results shown in Fig. 6 *a*.

diffraction geometry is shown in Fig. 8 *a* for both DMPC and SARS-CoV E protein at $P/L = 1/10$ (iodinated) as a function of lateral momentum transfer $q_{\|}$. Similar curves were obtained in the case of the noniodinated protein, and for the entire P/L sample series. With increasing P/L, the fluid correlation peak sharpens and moves to higher $q_{\|}$. At the same time, another component of lipids seems to produce a weak maximum at smaller $q_{\|}$, which is less pronounced. Note that wide-angle scattering of thin lipid films at in-house sources is difficult, yet the general trend is already very clear

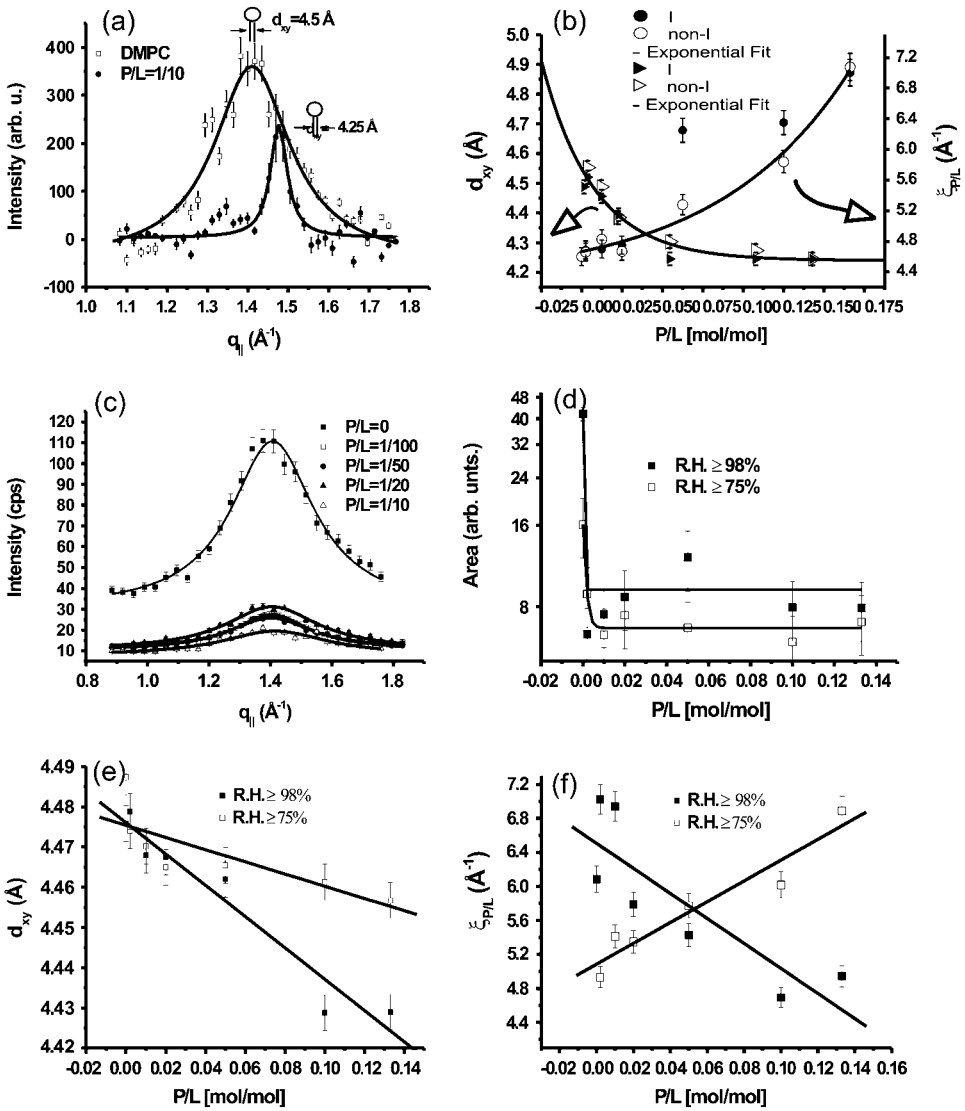

FIGURE 8 (*a*) Grazing incidence scattering curves measured around the acyl chain ordering peak ($T = 28°C$). A pure DMPC curve is compared to a curve of a lipid/protein mixture at $P/L = 1/10$, both plotted as a function of lateral momentum transfer $q_{\|}$. For $P/L = 1/10$, a sharpening and shift of the peak toward higher $q_{\|}$ indicates a more ordered chain packing. The presented curves are corrected for the background scattering, then fitted with Lorentzian function. (*b*) The nearest-neighbor distance and the correlation length as a function of P/L for both labeled and unlabeled samples along with empirical fits obtained form curves similar to that represented in panel *a*. (*c*) Same as in panel *a* but at high hydration and temperature ($T = 45°C$ and $R.H. = 98\%$). A pure DMPC curve is compared to curves of different lipid/protein mixtures in the fluid state, both plotted as a function of lateral momentum transfer $q_{\|}$. A large drop in the intensity is observed even at small protein concentrations. (*d*) The area under each scattering curve obtained from Lorentzian fits plotted on log scale as a function of P/L. (*e*) The nearest-neighbor distance as a function of P/L along with linear fits. (*f*) The correlation length as a function of P/L for the two hydration levels probed.

from the data presented. The scans were taken using a home-built diffractometer with a sealed tube of Cu K_α (i.e., λ = 1.54 Å) radiation, equipped with a collimating x-ray multilayer, motorized slits, and a fast scintillation counter. The setup is described in detail elsewhere (33). The samples were placed horizontally at the bottom of the chamber, and the temperature was set to 28°C.

Lorentzian fits to the scattering distribution data were performed for each *P/L* (i.e., see solid line in Fig. 8 *a*) to quantify the peak position $q_0(P/L)$ (not shown), correlation length $\xi_r(P/L)$ = 1/HWHM (half width at half maximum), and, consequently, the nearest-neighbor distance of acyl chains d_{xy} (i.e., $2\pi/q_0$). A graph of these quantities as a function of *P/L* is given in Fig. 8 *b*. It becomes clear that SARS-CoV E protein affects the ordering of the acyl tails in a dramatic way, even at relatively small concentrations. This implies that the protein changes the state of the bilayer in its vicinity over some range, and not only locally. Upon increase of the protein concentration, the peak shifts to larger q_0 values (e.g., smaller average next-neighbor distance d_{xy}), indicating a better ordered packing of the acyl chains. However, the observed shift in peak position and the increase in $\xi_r(P/L)$ shown in Fig. 8, *a* and *b*, could also be due to a shift of the main phase transition temperature. It is not clear that all samples, in particular those at high *P/L*, are in the fluid state at these temperatures. Since the chain correlation maximum at higher temperature deep in the fluid phase was hardly visible at the in-house diffractometer, we performed additional experiments using synchrotron radiation, for intensity reasons and better signal-to-noise ratios. These experiments were carried out at the D4 station of the Doris III storage ring of HASYLAB/DESY Hamburg, using a photon energy of 20 keV. Importantly, in contrast to Fig. 8, *a* and *b*, the samples were now heated up in the chamber to the same temperatures as in the reflectivity measurements to really ensure that the samples were all in the fluid state. In addition, the higher water-swelling states were achieved (periodicity $d \simeq 59$Å for pure DMPC). A huge decrease in the scattering intensity with *P/L* is observed even at small protein concentrations, pointing toward a strong disordering effect of the SARS-CoV E protein on acyl chain ordering in the fluid phase, see Fig. 8 *c*. For comparison, the measurements were tested at two levels of hydration, one imposed by a pure water reservoir in the chamber, and one by a saturated NaCl solution. Fig. 8 *e* shows an approximately linear decrease of the nearest-neighbor distance of acyl chains as a function of *P/L*, which is stronger at higher hydration, but much smaller than in Fig. 8 *b*. This comparison supports the assumption that the higher *P/L* samples at T = 28°C in Fig. 8 *b* were already in the gel phase. Note that it is not uncommon that the main phase transition changes with *P/L*. It is also important to point out that the changes in peak position are small (in the fluid phase) compared to the peak width. Finally, Fig. 8 shows the corresponding correlation lengths computed from the half width at half maximum values. The samples hydrated from salt solution show an increase in the ordering, analogous to the results for $T = 28$°C in the vicinity of the phase transition. Contrarily, the correlation length of the highly hydrated samples decreases with *P/L*. In summary, the gel and fluid phases behave quite differently. The main effect is always a strong decrease in scattering intensity. For high temperatures and high hydration a slight decrease in the correlation length and the average next-neighbor distance is observed. This is the most relevant regime, since the SARS-CoV E protein is in the inserted-hairpin state under these conditions.

SUMMARY AND CONCLUSIONS

The results show that incorporating the SARS-CoV E protein in the DMPC bilayers in the fluid phase induces significant changes in the bilayer structure. These changes are nonlocal in the sense that at small *P/L* the effect grows stronger in proportion to the lipids that locally surround the protein. This can be well understood since a local perturbation in the bilayer is generally accompanied by a nonlocal strain fields that relaxes the perturbation over some length. Such an effect has been observed experimentally for the antibiotic peptide Magainin 2 (39), and has been predicted theoretically based on bilayer elasticity models (40). In general terms, a hydrophobic mismatch of a transmembrane helix can be the source of such a perturbation. In the case described here, the experimental evidence gives a consistent picture in that both bilayer thickening and a decrease in the acyl chain distance are observed. These two phenomena occur simultaneously, since the free energy associated with the interaction between the chains is minimized if the density in the acyl chains is preserved. Thus, to increase bilayer thickness, the chains must necessarily approach. Near the gel phase they also become stretched at high *P/L*, most likely by an increase in the main phase transition.

In light of these results, let us consider possible molecular conformations. From previous FTIR results (20), we know that the protein helices are oriented perpendicular. From the density profiles of the iodinated protein, we know that the Phe-23 group is located at the hydrophilic/hydrophobic interface of the bilayer, at least at high hydration. This has led us to conclude that the protein forms a small alpha-helical hairpin. This is supported by the fact that, corresponding to 26 amino acids, a total transmembrane length of ~39 Å would lead to an impossibly high hydrophobic mismatch for a transmembrane helix. These values would be applicable, assuming that the entire hydrophobic part of SARS-CoV E forms an α-helix with each amino acid contributing an axial length of 1.5 Å (41). In general, protein- or peptide-lipid complexes are expected to respond to such an energetically unfavorable mismatch situation in a number of ways, depending on the molecular details of the system. The polypeptides can tilt or kink when their TM hydrophobic length is too long to match the bilayer, thus reducing their

effective length. In the opposite situation, a TM helix could adopt a more extended conformation or a nontransmembrane orientation (42–44). Alternatively, the lipid bilayer could respond to the mismatch situation by ordering or disordering their acyl chains or changing the bilayer's curvature (45,46). In our case, it seems that both the protein and the membrane responded to this unfavorable situation. Namely, the protein adopted a hairpin conformation, with two short helices of 13 amino acids corresponding to 20 Å. At the same time the membrane changed its thickness due to the presence of SCoV E protein.

For illustration, let us sketch different models in the light of these results, to determine which configurations could possibly encompass both an inserted hairpin structure and the bilayer thickening, and which configurations can be ruled out. The first model illustrated in Fig. 9 *a* shows the protein in the hairpin confirmation partly spanning the hydrophobic core of the bilayer. This would explain the FTIR and x-ray results on the protein conformation, but not why the bilayer would tend to thicken. It is also unclear in this case how the polar C- and N-termini can be encompassed in the hydrophobic core. In Fig. 9 *b*, the same conformation, with two hairpins forming a homodimmer, is sketched. Our experiments can so far not distinguish between Fig. 9, *a* and *b*, but the problems associated with Fig. 9 *a* obviously also apply here. The models shown in Fig. 9, *c* and *d*, follow from Fig. 9, *a* and *b*, respectively, if the bilayer thickness is allowed to thin to match the hydrophobic length of the hairpin, so that the polar ends are facing the other side of the bilayer. Obviously the required thinning would be too large and can be ruled out, just as the required thickness for one long TM helix would be too large (not shown). Finally, the thickening observed here directly rules out configurations *a–d* in Fig. 9. Finally, Fig. 9, *e* and *f*, shows homodimer configurations, in which the proteins associate not laterally but vertically. Again, simple stacking of two opposing hairpins such as the configuration shown in Fig. 9 *e* is unlikely, since the required thickness may be too high. Contrarily, Fig. 9 *f*, with the two opposing hairpins turned by 90° and inserted seems to be possible based on simple thickness considerations. This putative model assumes that the end termini are packed together to suppress the unfavored interactions between them and the acyl chains. The model would be in agreement with a small positive hydrophobic mismatch, which could explain the observed changes in the density profile and the acyl-chain scattering. Note that the transition between Fig. 9, *e* and *f*, is somewhat continuous depending on the degree of insertion. In conclusion, the reflectivity results, together with the chain correlation measurements, would be in line with Fig. 9, *e* and *f*, with hydrophobic mismatch considerations favoring Fig. 9 *f*.

Finally, in this study, we did not find any evidence for a destabilization of the bilayer. In fact, nonspecular reflectivity (diffuse scattering), as mapped by a two-dimensional CCD camera in the geometry of grazing incidence small-angle scattering, excludes any dramatic increase of bilayer corrugation or fluctuations with *P/L*. Thus the bilayers in the oriented stacks are found to be quasiplanar with the presence of the usual thermal fluctuations (47). A more quantitative analysis in the next step could quantify the associated changes in the elastic constants, such as the bending rigidity. However, an instability can already be ruled out from inspection of the raw data. At the same time SCoV E protein is known to play a role in virus budding. Therefore, this phenomenon must be linked to an asymmetric embedding SCoV E protein in the external leaflet of the bilayer that may perturb the membrane and also change its permeability. In situ experiments with vesicles and asymmetric embedding of proteins in model systems could help to address this question and may be helpful in understanding the effect of the SCoV E protein on the formation of ion channels and budding.

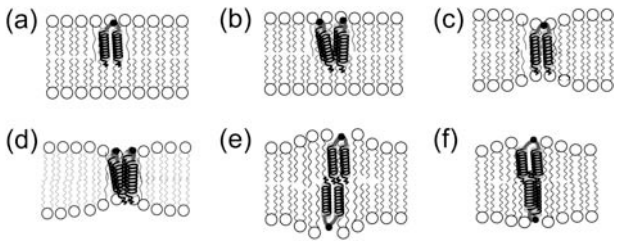

FIGURE 9 Cartoon representation of different possible models of SARS-CoV E protein structure and membrane topology. (*a*) Monomeric E protein inserted into the lipid bilayer membrane. This model suggests that the TMD partially spans the lipid bilayer as a hairpin. (*b*) The same as in *a* but two hairpins forming a homodimer. (*c*) The same as in *a*, with the lipid bilayer thickness adapted to minimize hydrophobic mismatch. (*d*) The same as *b*, but again with the lipid bilayer thickness adapted to minimize hydrophobic mismatch. (*e*) Vertical association of two hairpins to homodimers. The vertical thickness is adapted to the bilayer thickness by intercalation of the two hairpins. (*f*) Similar to *e* but with the bilayer thickness increased to match the length of two vertically stacked hairpins.

We thank HASYLAB/DESY for beam time and D. Novikov for help at D4.

We gratefully acknowledge financial support from the Deutsche Forschungsgemeinschaft through the German-Israel-Palestine trilateral project SA 7772/6-1.

REFERENCES

1. Poutanen, S. M., D. E. Low, B. Henry, S. Finkelstein, D. Rose, K. Green, R. Tellier, R. Draker, D. Adachi, M. Ayers, A. K. Chan, D. M. Skowronski, et al. 2003. Identification of severe acute respiratory syndrome in Canada. *N. Engl. J. Med.* 348:1995–2005.
2. Lee, N., D. Hui, A. Wu, P. Chan, P. Cameron, G. M. Joynt, A. Ahuja, M. Y. Yung, C. B. Leung, K. F. To, S. F. Lui, C. C. Szeto, et al. 2003. A major outbreak of severe acute respiratory syndrome in Hong Kong. *N. Engl. J. Med.* 348:1986–1994.
3. Peiris, J., S. T. Lai, L. L. Poon, Y. Guan, L. Y. Yam, W. Lim, J. Nicholls, W. K. Yee, W. W. Yan, M. T. Cheung, V. C. Cheng, K. H. Chan, et al. 2003. Coronavirus as a possible cause of severe acute respiratory syndrome. *Lancet.* 361:1319–1325.

4. Drosten, C., S. Gunther, W. Preiser, S. van der Werf, H. R. Brodt, S. Becker, H. Rabenau, M. Panning, L. Kolesnikova, R. A. Fouchier, A. Berger, A. M. Burguiere, et al. 2003. Identification of a novel coronavirus in patients with severe acute respiratory syndrome. *N. Engl. J. Med.* 348:1967–1976.

5. Ksiazek, T. G., D. Erdman, C. S. Goldsmith, S. R. Zaki, T. Peret, S. Emery, S. Tong, C. Urbani, J. A. Comer, W. Lim, P. E. Rollin, S. F. Dowell, et al. 2003. A novel coronavirus associated with severe acute respiratory syndrome. *N. Engl. J. Med.* 348:1953–1966.

6. Marra, M. A., S. J. Jones, C. R. Astell, R. A. Holt, A. Brooks-Wilson, Y. S. Butterfield, J. Khattra, J. K. Asano, S. A. Barber, S. Y. Chan, A. Cloutier, S. M. Coughlin, et al. 2003. The genome sequence of the SARS-associated coronavirus. *Science.* 300:1399–1404.

7. Rota, P. A., M. S. Oberste, S. S. Monroe, W. A. Nix, R. Campagnoli, J. P. Icenogle, S. Penaranda, B. Bankamp, K. Maher, M. H. Chen, S. Tong, A. Tamin, et al. 2003. Characterization of a novel coronavirus associated with severe acute respiratory syndrome. *Science.* 300:1394–1399.

8. Kuo, L., and P. S. Masters. 2003. The small envelope protein E is not essential for murine coronavirus replication. *J. Virol.* 77:4597–4608.

9. Bos, E. C., W. Luytjes, H. V. van der Meulen, H. K. Koerten, and W. J. Spaan. 1996. The production of recombinant infectious DI-particles of a murine coronoavirus in the absence of helper virus. *Virology.* 218:52–60.

10. Vennema, H., G. J. Godeke, J. W. Rossen, W. F. Voorhout, M. C. Horzinek, D. J. Opstelten, and P. J. Rottier. 1996. Nucleocapsid-independent assembly of coronavirus-like particles by co-expression of viral envelope protein genes. *EMBO J.* 15:2020–2028.

11. Lim, K. P., and D. X. Liu. 2001. The missing link in coronavirus assembly. Retention of the avian coronavirus infectious bronchitis virus envelope protein in the pre-Golgi compartments and physical interaction between the envelope and membrane proteins. *J. Biol. Chem.* 276:17515–17523.

12. Raamsman, M. J., J. K. Locker, A. de Hooge, A. A. de Vries, G. Griffiths, H. Vennema, and P. J. Rottier. 2000. Characterization of coronavirus mouse hepatitis virus strian A59 small membrane protein E. *J. Virol.* 74:2333–2342.

13. An, S., C. J. Yu, J. L. Leibowitz, and S. Makino. 1999. Induction of apoptosis in murine coronavirus-infected cultured cells and demonstration of E protein as an apoptosis inducer. *J. Virol.* 73:7853–7859.

14. Chen, C. J., S. An, and S. Makino. 2001. Induction of apoptosis in murine coronavirus-infected 17C1–1 cells. *Adv. Exp. Med. Biol.* 494:615–620.

15. Baudoux, P., C. Carrat, L. Besnardeau, B. Charley, and H. Luade. 1998. Coronavirus pseudoparticles formed with recombinant M and E proteins induce alpha interferon synthesis by leukocytes. *J. Virol.* 72:8636–8643.

16. Corse, E., and C. E. Machmaer. 2000. Infectious bronchitis virus E protein is targeted to the Golgi complex and directs release of virus-like particles. *J. Virol.* 74:4319–4326.

17. Maeda, J., A. Maeda, and S. Makino. 1999. Release of coronavirus E protein in membrane vesicles from virus-infected cells and E protein-expressing cells. *Virology.* 263:265–272.

18. Godet, M., R. L'Haridon, J. F. Vautherot, and H. Laude. 1992. TGEV coronavirus ORF4 encodes a membrane protein that is incorporated into virions. *Virology.* 188:666–675.

19. Arkin, I. T., and A. T. Brunger. 1998. Statistical analysis of predicted transmembrane alpha-helices. *Biochim. Biophys. Acta.* 1429:113–128.

20. Arbely, A., Z. Khattari, G. Brotons, M. Akkawi, T. Salditt, and I. T. Arkin. 2004. A Highly Unusual Palindromic Transmembrane Helical Hairpin Formed by SARS Coronavirus E Protein. *J. Mol. Biol.* 341:769–779.

21. Shen, X., J. H. Xue, C. Y. Yu, H. B. Luo, L. Kin, X. J. Yu, J. Chen, L. L. Chen, B. Xiong, L. D. Yue, J. H. Cai, J. H. Shen, et al. 2003. Small envelope protein E of SARS: cloning, expression, purification, CD determination, and bioinformatics analysis. *Acta Pharmacol. Sin.* 24: 505–511.

22. Maeda, J., J. F. Repass, A. Maeda, and S. Makino. 2001. Membrane topology of coronavirus E protein. *Virology.* 281:541–570.

23. Torres, J., J. Wang, K. Parthasarathy, and D. X. Liu. 2005. The transmembrane oligomers of coronavirus protein E. *Biophys. J.* 88: 1283–1290.

24. Seul, M., and M. J. Sammon. 1990. Preparation of surfactant multilayer films on solid substrates by deposition from organic solution. *Thin Solid Films.* 185:287–305.

25. Salditt, T., C. Münster, Y. Lu, M. Vogel, W. Fenzl, and A. Souvorov. 1999. Specular and diffuse scattering of highly aligned phospholipids membranes. *Phys. Rev. E.* 60:7285–7289.

26. Münster, C., J. Lu, S. Schinzel, B. Bechinger, and T. Salditt. 2000. Grazing incidence x-ray diffraction of highly aligned phospholipid membranes containing antimicrobial peptides magainin 2. *Eur. Biophys. J.* 28:683–688.

27. Brotons, G., T. Salditt, M. Dubois, and Th. Zemb. 2003. Highly oriented, charged multilamellar membranes osmotically stressed by a polyelectrolyte of same sign. *Langmuir.* 19:8235–8244.

28. Salditt, T., C. Li, A. Spaar, and U. Mennicke. 2002. X-ray reflectivity of solid-supported multilamellar membranes. *Eur. Phys. J. E.* 7:105–116.

29. Braslau, A., P. S. Pershan, G. Swislow, B. M. Ocko, and J. Als-Nielsen. 1988. Capillary waves on the surface of simple liquids measured by x-ray reflectivity. *Phys. Rev. A.* 38:2457–2470.

30. Tristram-Nagle, S., H. I. Petrache, and J. Nagle. 1998. Structure and interactions of fully hydrated dioleoylphosphatidylchline bilayers. *Biophys. J.* 75:917–925.

31. Gandhavadi, M., D. Allende, A. Vidal, S. A. Simon, and T. J. Mclntosh. 2002. Structure, composition, and peptide binding properties of detergent soluble bilayers and detergent resistant rafts. *Biophys. J.* 82:1469–1482.

32. Li, C., D. Constantin, and T. Salditt. 2004. Biomimetic membranes of lipid-peptide model systems prepared on solid support. *J. Phys. Cond. Matt.* 16:S2439–S2453.

33. Li, C. 2005. Strukturanalyse von Antibiotischen Peptides in Lipidmembranen mittels Röntgenreflektivität. Ph.D. thesis, Georg-August-Universität, Göttingen, Germany.

34. Wu, Y., K. He, S. J. Ludtke, and H. W. Huang. 1995. X-ray diffraction study of lipid bilayer membrane interacting with amphiphilic helical peptrides: diphytanoyl phosphatidylcholine with alamethicin at low concentrations. *Biophys. J.* 68:2361–2369.

35. Huang, H. W., and Y. Wu. 1991. Lipid-alamethicin interactions influence alamethicin orientation. *Biophys. J.* 60:1079–1087.

36. Ludtke, S., K. He, and H. W. Huang. 1995. Membrane thinning caused by magainin 2. *Biochemistry.* 34:16764–16769.

37. Chen, F.-Y., M.-T. Lee, and H. W. Huang. 2003. Evidence for membrane thinning effect as the mechanism for peptide-induced pore formation. *Biophys. J.* 84:3751–3758.

38. Khattari, Z., G. Brotons, E. Arbely, I. T. Arkin, T. H. Metzger, and T. Salditt. 2005. SARS E protein in phospholipid bilayers: an anomalous x-ray reflectivity study. *Physica B* (*Amsterdam*). 357:34–38.

39. Münster, C., A. Spaar, B. Bechinger, and T. Salditt. 1999. Magainin 2 in phospholipid bilayer: peptide orientation and lipid chain ordering studied by X-ray diffraction. *Biochim. Biophys. Acta.* 1562:37–44.

40. May, S. 2000. Theories on structural perturbations of lipid bilayers. *Curr. Opin. Colloid Interface Sci.* 5:244–249.

41. Killian, J. A., I. Salemink, M. R. R. De Planque, G. Lindblom, R. E. Koeppe 2nd, and D. V. Greathouse. 1996. Induction of nonbilayer structures in diacylphosphatidylcholine model membranes by transmembrane -helical peptides: importance of hydrophobic mismatch and proposed role of tryptophans. *Biochemistry.* 35:1037–1045.

42. Zhang, Y. P., R. N. Lewis, G. D. Henry, B. D. Sykes, R. S. Hodges, and R. N. McElhaney. 1995. Peptide models of helical hydrophobic transmembrane segments of membrane proteins. 1. Studies of the conformation, intrabilayer orientation, and amide hydrogen exchangeability of Ac-K2-(LA)12–K2-amide. *Biochemistry.* 34:2348–2361.

43. Zhang, Y. P., R. N. Lewis, R. S. Hodges, and R. N. McElhaney. 1995. Peptide models of helical hydrophobic transmembrane segments of membrane proteins. 2. Differential scanning calorimetric and FTIR spectroscopic studies of the interaction of Ac-K2-(LA)12–K2-amide with phosphatidylcholine bilayers. *Biochemistry*. 34:2362–2371.

44. Ren, J., Z. Wang, and E. London. 1996. Transmembrane orientation of hydrophobic helices is regulated both by the relationship of helix length to bilayer thickness and by the cholesterol concentration. *Biochemistry*. 36:10213–10220.

45. Mouritsen, O. G., and M. Bloom. 1984. Mattress model of lipid-protein interactions in membranes. *Biophys. J*. 46:141–153.

46. Owicki, J. C., M. W. Springgate, and H. M. McConnell. 1978. Theoretical study of protein-lipid interactions in bilayer membranes. *Proc. Natl. Acad. Sci. USA*. 75:1616–1619.

47. Salditt, T. 2003. Lipid-peptide interaction in oriented bilayers probed by interface-sensitive scattering methods. *Curr. Opin. Struct. Biol*. 13:467–478.